*Progress In Electromagnetics Research, PIER 67, 1–24, 2007*

# ELECTROMAGNETIC SCATTERING FROM ARBITRARILY SHAPED CHIRAL OBJECTS USING THE FINITE DIFFERENCE FREQUENCY DOMAIN METHOD

**L. Kuzu**

Department of Electrical Engineering and Computer Science
Syracuse University
Syracuse, NY 13244, USA

**V. Demir and A. Z. Elsherbeni**

Center of Applied Electromagnetics Systems Research (CAESR)
Department of Electrical Engineering
The University of Mississippi
University, MS 38677, USA

**E. Arvas**

Department of Electrical Engineering and Computer Science
Syracuse University
Syracuse, NY 13244, USA

**Abstract**—In this paper, finite difference frequency domain (FDFD) formulation has been developed for the analysis of electromagnetic wave interaction with chiral materials, and the validity of the formulation for three dimensional scattering problems has been confirmed by comparing the numerical results to exact or other numerical solutions. The influences of the chirality on the scattered field components are investigated. Numerical results for bistatic radar cross section (RCS) are presented and compared to reference solutions and it is found that the proposed FDFD method shows good agreement. It is realized that the presented method is relatively easy to program and can be applied to a wide variety of problems of complex and composite structures efficiently.

## 1. INTRODUCTION

Chiral material has been proposed for many applications due to its unique electromagnetic properties. Among them are antennas and arrays, antenna radomes, microstrip substrates and waveguides. Electromagnetic propagation in chiral medium differs from the behavior of simpler, isotropic materials in several ways [1]. A linearly polarized wave propagating in a chiral medium undergoes a rotation of its polarization. For example, scattered field from a homogeneous chiral cylinder has both TE and TM components even when the incident field is a pure TE or a pure TM wave incident on the cylinder [2].

The analysis of chiral materials has been an important topic in computational electromagnetics especially after artificial chiral materials have been manufactured in the microwave range in the last decade. Numerical analysis of chiral materials has been carried out using a variety of numerical methods, such as the method of moments (MoM) [2, 3], the finite-difference time-domain (FDTD) method [4, 5], boundary value solutions (BVS) [6] and so forth. In this paper, the finite difference frequency domain (FDFD) method has been used. FDFD method presents a versatile and relatively simple way of solving Maxwell's equations in the frequency domain, for arbitrary geometries. Although this method requires high memory and computer resources, in other words, it is computationally expensive, recent developments in the computer systems made possible the effective use of this numerical technique. One of the most important aspects of this method is flexibility; each cell can have a permittivity, permeability and chiral material properties independent of others. Therefore, it is easy to apply to non-uniform and frequency dependent media. Also it is not necessary to keep the grid spacing uniform. This is especially important when large objects with regions that contain small, complex geometries that require dense grids. Therefore, it can be applied to a wide variety of problems of complex and composite structures efficiently.

## 2. FORMULATION

In this paper, the field equations for scattering by chiral materials are developed for three-dimensional (3D) problems. The incident field expressions are also given. A perfectly matched layer surrounding the discretized solution space is also implemented to absorb the outgoing waves. The termination of the computational domain considered in this paper is an absorbing boundary condition (ABC), based on

the perfectly matched layer (PML) developed by Berenger [7]. The FDFD/PML solution procedure has been developed and applied for arbitrarily shaped 3D chiral objects.

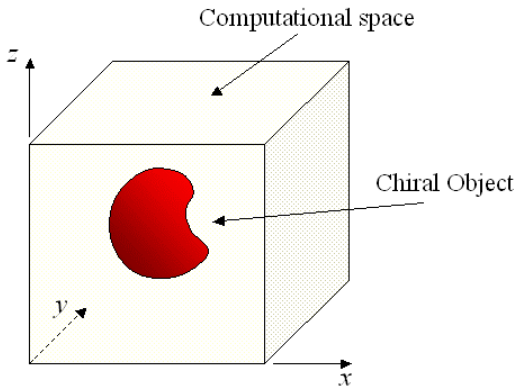


**Figure 1.** Problem geometry for a 3D chiral object.

Consider a chiral scatterer in free space as shown in Fig. 1. The following constitutive relations in the frequency domain can describe chiral materials:

$$\overline{D} = \varepsilon \overline{E} - j\kappa\sqrt{\varepsilon_o \mu_o}\overline{H}, \qquad \overline{B} = \mu \overline{H} + j\kappa\sqrt{\varepsilon_o \mu_o}\overline{E} \tag{1}$$

where $\kappa$ measures the chirality, $\varepsilon$ and $\mu$ are the dielectric and magnetic parameter of the media respectively [1]. The assumed time harmonic convention is $e^{+j\omega t}$. All material parameters are non-homogenuous and anisotropic in general. The Maxwell's equations in the frequency domain can be written as

$$\nabla \times \overline{E} = -j\omega \overline{B}, \qquad \nabla \times \overline{H} = +j\omega \overline{D}. \tag{2}$$

Substituting (1) into (2) gives

$$\nabla \times \overline{E} = -j\omega\mu \overline{H} + \frac{\omega\kappa}{c}\overline{E}, \tag{3a}$$

$$\nabla \times \overline{H} = +j\omega\varepsilon \overline{E} + \frac{\omega\kappa}{c}\overline{H}. \tag{3b}$$

Although both equations in (3) are continuous equations and are valid at every point in computational space, the position of the $\kappa$ in (3a) is different than that of (3b) when they are written for discrete grid points. The first is associated with $\overline{H}$, whereas the second one is with

$\overline{E}$. After this point, we will use different notations for them, namely $\kappa_h$ and $\kappa_e$.

The formulation developed in this paper is based on the scattered field formulation in which the total field is the sum of known incident and unknown scattered fields [8, 9]. Decomposing the total field into incident and scattered fields gives

$$\begin{aligned}\nabla\times\overline{E}_{inc}+\nabla\times\overline{E}_{scat} &= -j\omega\mu\overline{H}_{inc}+\frac{\omega\kappa_h}{c}\overline{E}_{inc}-j\omega\mu\overline{H}_{scat}+\frac{\omega\kappa_h}{c}\overline{E}_{scat}\\ \nabla\times\overline{H}_{inc}+\nabla\times\overline{H}_{scat} &= j\omega\varepsilon\overline{E}_{inc}+j\omega\varepsilon\overline{E}_{scat}+\frac{\omega\kappa_e}{c}\overline{H}_{inc}+\frac{\omega\kappa_e}{c}\overline{H}_{scat}.\end{aligned} \tag{4}$$

By definition, incident field satisfies Maxwell's equations in free space, so that

$$\begin{aligned}\nabla\times\overline{E}_{inc} &= -j\omega\mu_o\overline{H}_{inc}\\ \nabla\times\overline{H}_{inc} &= +j\omega\varepsilon_o\overline{E}_{inc}.\end{aligned} \tag{5}$$

Substituting (5) into (4) gives

$$\begin{aligned}\nabla\times\overline{E}_{scat}-\frac{\omega\kappa_h}{c}\overline{E}_{scat}+j\omega\mu\overline{H}_{scat} &= j\omega\left(\mu_o-\mu\right)\overline{H}_{inc}+\frac{\omega\kappa_h}{c}\overline{E}_{inc}\\ \nabla\times\overline{H}_{scat}-\frac{\omega\kappa_e}{c}\overline{H}_{scat}-j\omega\varepsilon\overline{E}_{scat} &= j\omega\left(\varepsilon-\varepsilon_o\right)\overline{E}_{inc}+\frac{\omega\kappa_e}{c}\overline{H}_{inc}.\end{aligned} \tag{6}$$

Decomposing the vector equations to $x$, $y$, and $z$ components, we obtain six scalar equations as follows:

$$\begin{aligned}&\frac{\partial E_{scat,z}}{\partial y}-\frac{\partial E_{scat,y}}{\partial z}-\frac{\omega\kappa_{hx}}{c}E_{scat,x}+j\omega\mu_x H_{scat,x}\\ &=j\omega\left(\mu_o-\mu_x\right)H_{inc,x}+\frac{\omega\kappa_{hx}}{c}E_{inc,x}\\ &\frac{\partial E_{scat,x}}{\partial z}-\frac{\partial E_{scat,z}}{\partial x}-\frac{\omega\kappa_{hy}}{c}E_{scat,y}+j\omega\mu_y H_{scat,y}\\ &=j\omega\left(\mu_o-\mu_y\right)H_{inc,y}+\frac{\omega\kappa_{hy}}{c}E_{inc,y}\\ &\frac{\partial E_{scat,y}}{\partial x}-\frac{\partial E_{scat,x}}{\partial y}-\frac{\omega\kappa_{hz}}{c}E_{scat,z}+j\omega\mu_z H_{scat,z}\\ &=j\omega\left(\mu_o-\mu_z\right)H_{inc,z}+\frac{\omega\kappa_{hz}}{c}E_{inc,z}\\ &\frac{\partial H_{scat,z}}{\partial y}-\frac{\partial H_{scat,y}}{\partial z}-\frac{\omega\kappa_{ex}}{c}H_{scat,x}-j\omega\varepsilon_x E_{scat,x}\\ &=j\omega\left(\varepsilon_x-\varepsilon_o\right)E_{inc,x}+\frac{\omega\kappa_{ex}}{c}H_{inc,x}\end{aligned} \tag{7}$$

$$\begin{aligned}
&\frac{\partial H_{scat,x}}{\partial z}-\frac{\partial H_{scat,z}}{\partial x}-\frac{\omega\kappa_{ey}}{c}H_{scat,y}-j\omega\varepsilon_y E_{scat,y}\\
&=j\omega\left(\varepsilon_y-\varepsilon_o\right)E_{inc,y}+\frac{\omega\kappa_{ey}}{c}H_{inc,y}\\
&\frac{\partial H_{scat,y}}{\partial x}-\frac{\partial H_{scat,x}}{\partial y}-\frac{\omega\kappa_{ez}}{c}H_{scat,z}-j\omega\varepsilon_z E_{scat,z}\\
&=j\omega\left(\varepsilon_z-\varepsilon_o\right)E_{inc,z}+\frac{\omega\kappa_{ex}}{c}H_{inc,z}
\end{aligned} \tag{8}$$

The set of equations of (7) and (8) forms the basis of the FDFD numerical algorithm for electromagnetic wave interactions with arbitrarily shaped three-dimensional chiral objects. Therefore they can be used to construct the 3D, 2D and 1D FDFD chiral equations.

In order to make the computational space finite, a perfectly matched layer surrounding the discretized computational space should be implemented to absorb the outgoing waves. The termination of the computational domain is based on the perfectly matched layer (PML) approach developed by Berenger [7]. Following notations in [10] the unsplit-field PML equations can be written as:

$$\begin{aligned}
H_x&=\frac{1}{(j\omega\mu_o+\sigma_z^m)}\frac{\partial E_y}{\partial z}-\frac{1}{\left(j\omega\mu_o+\sigma_y^m\right)}\frac{\partial E_z}{\partial y}\\
H_y&=\frac{1}{(j\omega\mu_o+\sigma_x^m)}\frac{\partial E_z}{\partial x}-\frac{1}{(j\omega\mu_o+\sigma_z^m)}\frac{\partial E_x}{\partial z}\\
H_z&=\frac{1}{\left(j\omega\mu_o+\sigma_y^m\right)}\frac{\partial E_x}{\partial y}-\frac{1}{(j\omega\mu_o+\sigma_x^m)}\frac{\partial E_y}{\partial x}
\end{aligned} \tag{9}$$

$$\begin{aligned}
E_x&=\frac{1}{\left(j\omega\varepsilon_o+\sigma_y^e\right)}\frac{\partial H_z}{\partial y}-\frac{1}{(j\omega\varepsilon_o+\sigma_z^e)}\frac{\partial H_y}{\partial z}\\
E_y&=\frac{1}{(j\omega\varepsilon_o+\sigma_z^e)}\frac{\partial H_x}{\partial z}-\frac{1}{(j\omega\varepsilon_o+\sigma_x^e)}\frac{\partial H_z}{\partial x}\\
E_z&=\frac{1}{(j\omega\varepsilon_o+\sigma_x^e)}\frac{\partial H_y}{\partial x}-\frac{1}{\left(j\omega\varepsilon_o+\sigma_y^e\right)}\frac{\partial H_x}{\partial y}
\end{aligned} \tag{10}$$

where in the PML region

$$\begin{aligned}
\varepsilon_x&=\varepsilon_o+\frac{\sigma_x^e}{j\omega} \qquad \mu_x=\mu_o+\frac{\sigma_x^m}{j\omega}\\
\varepsilon_y&=\varepsilon_o+\frac{\sigma_y^e}{j\omega} \qquad \mu_y=\mu_o+\frac{\sigma_y^m}{j\omega}\\
\varepsilon_z&=\varepsilon_o+\frac{\sigma_z^e}{j\omega} \qquad \mu_z=\mu_o+\frac{\sigma_z^m}{j\omega}
\end{aligned} \tag{11}$$

and outside the PML region

$$\begin{aligned} \varepsilon &= \varepsilon_x = \varepsilon_y = \varepsilon_z = \varepsilon' - j\varepsilon'' \\ \mu &= \mu_x = \mu_y = \mu_z = \mu' - j\mu''. \end{aligned} \tag{12}$$

Note that if the medium is lossy then the real part of the $\varepsilon$ represents the dielectric constant of the medium and the imaginary part of the $\varepsilon$ represents the loss tangent of the medium. Similarly, the real part of the $\mu$ represents the magnetic permeability of the medium and the imaginary part of it represents the magnetic loss of the medium.

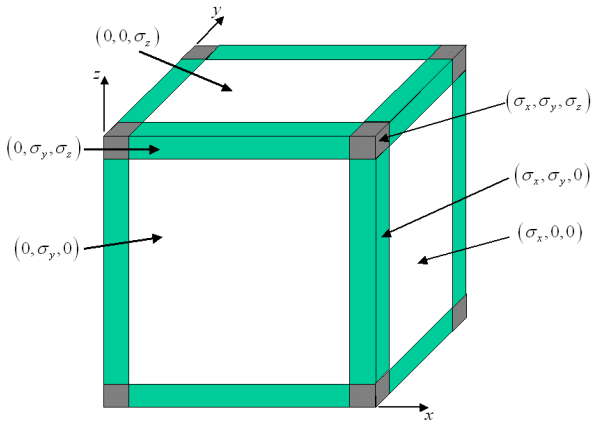


**Figure 2.** 3D structure of PML layers.

We can combine PML equations with chiral equations to obtain one set of equations which is valid both for the PML region and the non-PML region in the computational space as:

$$\begin{aligned} &H_{scat,\,x} - \frac{j}{\omega\mu_{xy}}\frac{\partial E_{scat,\,z}}{\partial y} + \frac{j}{\omega\mu_{xz}}\frac{\partial E_{scat,\,y}}{\partial z} + \frac{j\kappa_{hx}}{\mu_{xi}c}E_{scat,\,x} \\ &= \frac{(\mu_o - \mu_{xi})}{\mu_{xi}}H_{inc,\,x} - \frac{j\kappa_{hx}}{\mu_{xi}c}E_{inc,\,x} \end{aligned}$$

$$\begin{aligned} &H_{scat,\,y} - \frac{j}{\omega\mu_{yz}}\frac{\partial E_{scat,\,x}}{\partial z} + \frac{j}{\omega\mu_{yx}}\frac{\partial E_{scat,\,z}}{\partial x} + \frac{j\kappa_{hy}}{\mu_{yi}c}E_{scat,\,y} \\ &= \frac{(\mu_o - \mu_{yi})}{\mu_{yi}}H_{inc,\,y} - \frac{j\kappa_{hy}}{\mu_{yi}c}E_{inc,\,y} \end{aligned}$$

$$\begin{aligned} &H_{scat,\,z} - \frac{j}{\omega\mu_{zx}}\frac{\partial E_{scat,\,y}}{\partial x} + \frac{j}{\omega\mu_{zy}}\frac{\partial E_{scat,\,x}}{\partial y} + \frac{j\kappa_{hz}}{\mu_{zi}c}E_{scat,\,z} \\ &= \frac{(\mu_o - \mu_{zi})}{\mu_{zi}}H_{inc,\,z} - \frac{j\kappa_{hz}}{\mu_{zi}c}E_{inc,\,z} \end{aligned} \tag{13}$$

where in the non-PML region

$$\begin{gathered} \mu_{xi} = \mu_x, \quad \mu_{xy} = \mu_x, \quad \mu_{xz} = \mu_x, \\ \mu_{yi} = \mu_y, \quad \mu_{yx} = \mu_y, \quad \mu_{yz} = \mu_y, \\ \mu_{zi} = \mu_z, \quad \mu_{zx} = \mu_z, \quad \mu_{zy} = \mu_z, \\ \kappa_{hx} = \kappa_{hz} = \kappa_{hy} = \kappa \end{gathered} \tag{14}$$

and in the PML region

$$\begin{gathered} \mu_{xi} = \mu_o, \quad \mu_{xy} = \mu_o + \frac{\sigma_y^m}{j\omega}, \quad \mu_{xz} = \mu_o + \frac{\sigma_z^m}{j\omega}, \\ \mu_{yi} = \mu_o, \quad \mu_{yz} = \mu_o + \frac{\sigma_x^m}{j\omega}, \quad \mu_{yz} = \mu_o + \frac{\sigma_z^m}{j\omega}, \\ \mu_{zi} = \mu_o, \quad \mu_{zx} = \mu_o + \frac{\sigma_x^m}{j\omega}, \quad \mu_{zy} = \mu_o + \frac{\sigma_y^m}{j\omega}, \\ \kappa_{hx} = \kappa_{hy} = \kappa_{hz} = 0. \end{gathered} \tag{15}$$

Similarly, we can write the three-dimensional chiral equations with PML for $\overline{E}$ field components using (8) leaving the incident fields on the right, as:

$$\begin{aligned} &E_{scat,\,x} - \frac{1}{j\omega\varepsilon_{xy}}\frac{\partial H_{scat,\,z}}{\partial y} + \frac{1}{j\omega\varepsilon_{xz}}\frac{\partial H_{scat,\,y}}{\partial z} + \frac{\kappa_{ex}}{j\varepsilon_{xi}c}H_{scat,\,x} \\ &= \frac{(\varepsilon_o - \varepsilon_{xi})}{\varepsilon_{xi}}E_{inc,\,x} - \frac{\kappa_{ex}}{j\varepsilon_{xi}c}H_{inc,\,x} \\ &E_{scat,\,y} - \frac{1}{j\omega\varepsilon_{yz}}\frac{\partial H_{scat,\,x}}{\partial z} + \frac{1}{j\omega\varepsilon_{yx}}\frac{\partial H_{scat,\,z}}{\partial x} + \frac{\kappa_{ey}}{j\varepsilon_{yi}c}H_{scat,\,y} \\ &= \frac{(\varepsilon_o - \varepsilon_{yi})}{\varepsilon_{yi}}E_{inc,\,y} - \frac{\kappa_{ey}}{j\varepsilon_{yi}c}H_{inc,\,y} \\ &E_{scat,\,z} - \frac{1}{j\omega\varepsilon_{zx}}\frac{\partial H_{scat,\,y}}{\partial x} + \frac{1}{j\omega\varepsilon_{zy}}\frac{\partial H_{scat,\,x}}{\partial y} + \frac{\kappa_{ez}}{j\varepsilon_{zi}c}H_{scat,\,z} \\ &= \frac{(\varepsilon_o - \varepsilon_{zi})}{\varepsilon_{zi}}E_{inc,\,z} - \frac{\kappa_{ez}}{j\varepsilon_{zi}c}H_{inc,\,z} \end{aligned} \tag{16}$$

where in the non-PML region

$$\begin{aligned} \varepsilon_{xy} = \varepsilon_x, \quad \varepsilon_{xz} = \varepsilon_x, \quad \varepsilon_{xi} = \varepsilon_x, \\ \varepsilon_{yx} = \varepsilon_y, \quad \varepsilon_{yz} = \varepsilon_y, \quad \varepsilon_{yi} = \varepsilon_y, \\ \varepsilon_{zx} = \varepsilon_z, \quad \varepsilon_{zy} = \varepsilon_z, \quad \varepsilon_{zi} = \varepsilon_z, \\ \kappa_{ex} = \kappa_{ey} = \kappa_{ez} = \kappa \end{aligned} \tag{17}$$

and in the PML region

$$\begin{aligned} \varepsilon_{xy} = \varepsilon_o + \frac{\sigma_y^e}{j\omega}, \quad \varepsilon_{xz} = \varepsilon_o + \frac{\sigma_z^e}{j\omega}, \quad \varepsilon_{xi} = \varepsilon_o, \\ \varepsilon_{yx} = \varepsilon_o + \frac{\sigma_x^e}{j\omega}, \quad \varepsilon_{yz} = \varepsilon_o + \frac{\sigma_z^e}{j\omega}, \quad \varepsilon_{yi} = \varepsilon_o, \\ \varepsilon_{zx} = \varepsilon_o + \frac{\sigma_x^e}{j\omega}, \quad \varepsilon_{zy} = \varepsilon_o + \frac{\sigma_y^e}{j\omega}, \quad \varepsilon_{zi} = \varepsilon_o, \\ \kappa_{ex} = \kappa_{ey} = \kappa_{ez} = 0. \end{aligned} \tag{18}$$

The finite difference method will be used to solve (13) and (16).

### 2.1. Incident Field Expressions

The incident plane wave shown in Fig. 3 can be implemented as

$$E = \left( E_\theta \hat{\theta} + E_\phi \hat{\phi} \right) e^{-j\vec{k}\cdot\vec{r}} \tag{19}$$

where $E_\theta$ and $E_\phi$ specify the amplitude of the plane wave. One can write the propagation and position vectors, respectively, as

$$\vec{k} = -k \left( \hat{x} \sin\theta_{inc} \cos\phi_{inc} + \hat{y} \sin\theta_{inc} \sin\phi_{inc} + \hat{z} \cos\theta_{inc} \right), \tag{20}$$

$$\vec{r} = \hat{x}x + \hat{y}y + \hat{z}z. \tag{21}$$

where $k = \frac{\omega}{c}$ where $c = \frac{1}{\sqrt{\mu_o \varepsilon_o}}$ is the speed of light. The incident plane wave comes from the direction where $(\theta, \phi) = (\theta_{inc}, \phi_{inc})$.

The position vector $\vec{r}$ is measured from the origin $(0, 0, 0)$ to the position of each electric and magnetic field component inside the computational domain. Both $E_\theta$ and $E_\phi$ have to be transformed to Cartesian coordinates in order to fit the Cartesian Yee grid to be used in the computational domain. Therefore the amplitudes of the incident plane waves in the $x$, $y$, and $z$ directions are calculated as follows:

$$E_{x0} = E_\theta \cos\theta_{inc} \cos\phi_{inc} - E_\phi \sin\phi_{inc} \tag{22a}$$

$$E_{y0} = E_\theta \cos\theta_{inc} \sin\phi_{inc} + E_\phi \cos\phi_{inc} \tag{22b}$$

$$E_{z0} = -E_\theta \sin\theta_{inc}. \tag{22c}$$

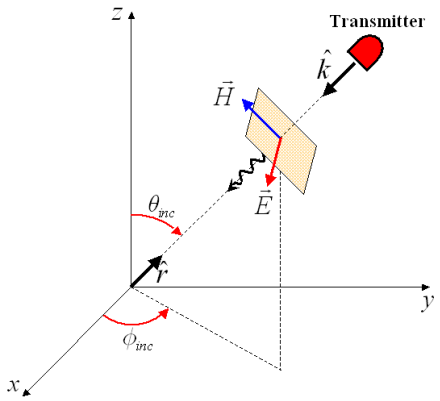


**Figure 3.** Incident plane wave in a 3D space.

The corresponding magnetic field components are

$$H_{x0} = \frac{1}{\eta}\left(E_\theta \cos\theta_{inc}\cos\phi_{inc} + E_\theta \sin\phi_{inc}\right) \tag{23a}$$

$$H_{y0} = \frac{1}{\eta}\left(E_\phi \cos\theta_{inc}\sin\phi_{inc} - E_\theta \cos\phi_{inc}\right) \tag{23b}$$

and

$$H_{z0} = \frac{1}{\eta}\left(-E_\phi \sin\theta_{inc}\right). \tag{23c}$$

After performing the dot product of (20) and (21) and using the field amplitudes (22) and (23), we obtain the incident field components for 3D problems as follows:

$$E_{inc,\,z} = (-E_\theta \sin\theta_{inc}) \; e^{+jk(x\sin\theta_{inc}\cos\phi_{inc} + y\sin\theta_{inc}\sin\phi_{inc} + z\cos\theta_{inc})} \tag{24a}$$

$$E_{inc,\,y} = (E_\theta \cos\theta_{inc}\sin\phi_{inc} + E_\phi \cos\phi_{inc}) \; e^{+jk(x\sin\theta_{inc}\cos\phi_{inc} + y\sin\theta_{inc}\sin\phi_{inc} + z\cos\theta_{inc})} \tag{24b}$$

$$E_{inc,\,x} = (E_\theta \cos\theta_{inc}\cos\phi_{inc} - E_\phi \sin\phi_{inc}) \; e^{+jk(x\sin\theta_{inc}\cos\phi_{inc} + y\sin\theta_{inc}\sin\phi_{inc} + z\cos\theta_{inc})} \tag{24c}$$

$$H_{inc,\,z} = \frac{1}{\eta}(-E_\phi \sin\theta_{inc}) \; e^{+jk(x\sin\theta_{inc}\cos\phi_{inc} + y\sin\theta_{inc}\sin\phi_{inc} + z\cos\theta_{inc})} \tag{24d}$$

$$H_{inc,y}=\frac{1}{\eta}\left(E_\phi \cos\theta_{inc}\sin\phi_{inc} - E_\theta \cos\phi_{inc}\right) \qquad (24e)$$
$$e^{+jk(x\sin\theta_{inc}\cos\phi_{inc}+y\sin\theta_{inc}\sin\phi_{inc}+z\cos\theta_{inc})}$$

$$H_{inc,x}=\frac{1}{\eta}\left(E_\phi \cos\theta_{inc}\cos\phi_{inc} + E_\phi \sin\phi_{inc}\right) \qquad (24f)$$
$$e^{+jk(x\sin\theta_{inc}\cos\phi_{inc}+y\sin\theta_{inc}\sin\phi_{inc}+z\cos\theta_{inc})}$$

where $\eta = \sqrt{\frac{\mu_o}{\varepsilon_o}}$ and $k$ are the intrinsic impedance and the wavenumber of the medium, respectively, where the incident field is excited (chosen as air), $\phi_{inc}$ and $\theta_{inc}$ are the incident angles with respect to the $x$- and $z$-axes, respectively, and $x$, $y$, and $z$ are the Cartesian coordinates.

## 2.2. Finite Difference Application

Maxwell's equations are discretized using a Yee cell as shown in Fig. 4. Therefore, the first step in the construction of the FDFD algorithm is the discretization of the computational space into cells and the definition of the locations of the electric and magnetic field vectors associated with each cell. Yee [11] developed an algorithm in which the electric and magnetic field vector components are located in a staggered fashion as shown in Fig. 4. The reason for the staggered grid is that when the curl operator is approximated using a difference formula, the resulting derivative is evaluated at a point that is in between the sample locations used in the difference formula. In each cell three electric field components and three magnetic field components are defined. They do

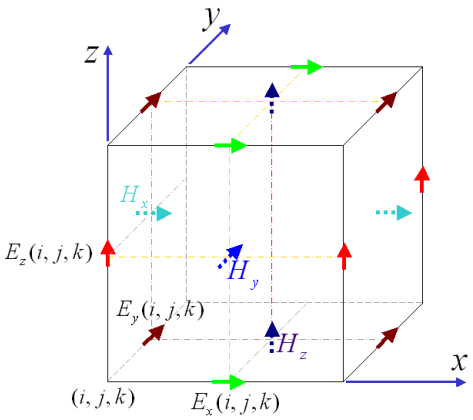


**Figure 4.** Yee cell demonstrating the positions of the $E$ and $H$ field vector components within a cubical grid.

not coincide with the nodes $(i, j, k)$ of the Cartesian grid. The electric field components are located at the centers of the edges of the cell and the magnetic field components are normal to the centers of the faces. This special configuration depicts Faraday's Law and Ampere's Law. In Figs. 4 and 5, it can be seen that each magnetic field vector component is surrounded by four electric field components forming a loop around it and simulating Faraday's law, and each electric field vector component is surrounded by four magnetic field components forming a loop around it and simulating Ampere's Law. Using this scheme, one can describe the explicit finite difference approximation of Maxwell's equations.

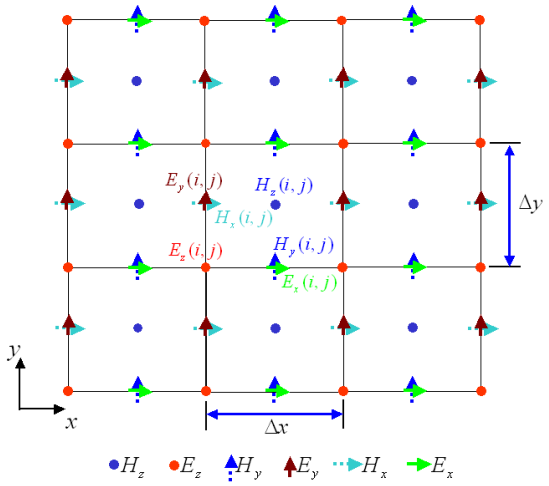


**Figure 5.** Top view of field components of a three dimensional FDFD grid.

In the three-dimensional Yee grid shown in Fig. 4, we apply finite difference method to (13) as follows

$$H_{scat,x}(i,j,k) + \frac{1}{j\omega\Delta y\mu_{xy}(i,j,k)} E_{scat,z}(i,\ j+1,\ k)$$
$$-\frac{1}{j\omega\Delta y\mu_{xy}(i,j,k)} E_{scat,z}(i,j,k) - \frac{1}{j\omega\Delta z\mu_{xz}(i,j,k)} E_{scat,y}(i,j,k+1)$$
$$+\frac{1}{j\omega\Delta z\mu_{xz}(i,j,k)} E_{scat,y}(i,j,k) - \frac{\kappa_{hx}(i,j,k)}{jc\mu_{xi}(i,j,k)} \frac{1}{8}$$

$$\begin{bmatrix} +E_{scat,\,x}(i,j,k)+E_{scat,\,x}(i-1,j,k) \\ +E_{scat,\,x}(i,j+1,k)+E_{scat,\,x}(i-1,j+1,k) \\ +E_{scat,\,x}(i,j,k+1)+E_{scat,\,x}(i,j+1,k+1) \\ +E_{scat,\,x}(i-1,j,k+1)+E_{scat,\,x}(i-1,j+1,k+1) \end{bmatrix}$$
$$= \frac{(\mu_o - \mu_{xi}(i,j,k))}{\mu_{xi}(i,j,k)} H_{inc,\,x}(i,j,k) + \frac{\kappa_{hx}(i,j,k)}{jc\mu_{xi}(i,j,,k)} \frac{1}{8}$$
$$\begin{bmatrix} +E_{inc,x}(i,j,k) + E_{inc,\,x}(i-1,j,k) \\ +E_{inc,x}(i,j+1,k)+E_{inc,\,x}(i-1,j+1,k) \\ +E_{inc,x}(i,j,k+1)+E_{inc,\,x}(i,j+1,k+1) \\ +E_{inc,x}(i-1,j,k+1)+E_{inc,\,x}(i-1,j+1,k+1) \end{bmatrix} \tag{25a}$$

$$H_{scat,y}(i,j,k) - \frac{\kappa_{hy}(i,j,k)}{jc\mu_{yi}(i,j,k)} \frac{1}{8}$$
$$\begin{bmatrix} +E_{scat,y}(i,j,k)+E_{scat,y}(i+1,j,k) \\ +E_{scat,y}(i,j-1,k)+E_{scat,y}(i+1,j-1,k) \\ +E_{scat,y}(i,j,k+1)+E_{scat,y}(i+1,j,k+1) \\ +E_{scat,y}(i,j-1,k+1)+E_{scat,y}(i+1,j-1,k+1) \end{bmatrix}$$
$$+\frac{1}{j\omega\Delta z\mu_{yz}(i,j,k)} E_{scat,\,x}(i,j,k+1) - \frac{1}{j\omega\Delta z\mu_{yz}(i,j,k)} E_{scat,\,x}(i,j,k)$$
$$-\frac{1}{j\omega\Delta x\mu_{yx}(i,j,k)} E_{scat,\,z}(i+1,j,k) + \frac{1}{j\omega\Delta x\mu_{yx}(i,j,k)} E_{scat,\,z}(i,j,k)$$
$$= \frac{(\mu_o - \mu_{yx}(i,j,k))}{\mu_{yi}(i,j,k)} H_{inc,y}(i,j,k) + \frac{\kappa_{hy}(i,j,k)}{jc\mu_{yi}(i,j,k)} \frac{1}{8}$$
$$\begin{bmatrix} +E_{inc,\,y}(i,j,k) + E_{inc,\,y}(i+1,\,j,\,k) \\ +E_{inc,\,y}(i,\,j-1,\,k) + E_{inc,\,y}(i+1,\,j-1,\,k) \\ +E_{inc,\,y}(i,\,j,\,k+1) + E_{inc,\,y}(i+1,\,j,\,k+1) \\ +E_{inc,\,y}(i,\,j-1,\,k+1) + E_{inc,\,y}(i+1,\,j-1,\,k+1) \end{bmatrix} \tag{25b}$$

$$H_{scat,\,z}(i,j,k) - \frac{\kappa_{hz}(i,j,k)}{jc\mu_{zi}(i,j,k)} \frac{1}{8}$$
$$\begin{bmatrix} +E_{scat,\,z}(i,j,k) + E_{scat,\,z}(i+1,\,j,\,k) \\ +E_{scat,\,z}(i,\,j+1,\,k) + E_{scat,\,z}(i+1,\,j+1,\,k) \\ +E_{scat,\,z}(i,\,j,\,k-1) + E_{scat,\,z}(i+1,\,j,\,k-1) \\ +E_{scat,\,z}(i,\,j+1,\,k-1) + E_{scat,\,z}(i+1,\,j+1,\,k-1) \end{bmatrix}$$
$$+\frac{1}{j\omega\Delta x\mu_{zx}(i,j,k)} E_{scat,y}(i+1,j,k) - \frac{1}{j\omega\Delta x\mu_{zx}(i,j,k)} E_{scat,\,y}(i,j,k)$$

$$
\begin{aligned}
&-\frac{1}{j\omega\Delta y\mu_{zy}(i,j,k)}E_{scat,x}(i,j{+}1,k)+\frac{1}{j\omega\Delta y\mu_{zy}(i,\ j,k)}E_{scat,\,x}(i,j,k)\\
&=\frac{(\mu_o-\mu_{zi}(i,j,k))}{\mu_{zi}(i,j,k)}H_{inc,z}(i,j,k)+\frac{\kappa_{hz}(i,j,k)}{jc\mu_{zi}(i,j,k)}\frac{1}{8}\\
&\left[\begin{array}{l}
+E_{inc,\,z}(i,j,k)+E_{inc,\,z}(i+1,\ j,\ k)\\
+E_{inc,\,z}(i,\ j+1,\ k)+E_{inc,\,z}(i+1,\ j+1,\ k)\\
+E_{inc,\,z}(i,\ j,\ k-1)+E_{inc,\,z}(i+1,\ j,\ k-1)\\
+E_{inc,\,z}(i,\ j+1,\ k-1)+E_{inc,\,z}(i+1,\ j+1,\ k-1)
\end{array}\right].
\end{aligned}
\tag{25c}
$$

Similarly, the finite difference equations representing (16) are given by

$$
\begin{aligned}
&E_{scat,\,x}(i,j,k)-\frac{1}{j\omega\Delta y\varepsilon_{xy}(i,j,k)}H_{scat,\,z}(i,j,k)\\
&+\frac{1}{j\omega\Delta y\varepsilon_{xy}(i,j,k)}H_{scat,z}(i,j{-}1,\ k)+\frac{1}{j\omega\Delta z\varepsilon_{xz}(i,j,k)}H_{scat,\,y}(i,j,k)\\
&-\frac{1}{j\omega\Delta z\varepsilon_{xz}(i,j,k)}H_{scat,y}(i,j,k{-}1)+\frac{\kappa_{ex}(i,j,k)}{j\varepsilon_{xi}(i,j,k)c}\frac{1}{8}\\
&\left[\begin{array}{l}
+H_{scat,\,x}(i,j,k)+H_{scat,\,x}(i,\ j,\ k-1)\\
+H_{scat,\,x}(i+1,\ j,\ k)+H_{scat,\,x}(i+1,\ j,\ k-1)\\
+H_{scat,\,x}(i,\ j-1,\ k)+H_{scat,\,x}(i,\ j-1,\ k-1)\\
+H_{scat,\,x}(i+1,\ j-1,\ k)+H_{scat,\,x}(i+1,\ j-1,\ k-1)
\end{array}\right]\\
&=\frac{(\varepsilon_o-\varepsilon_{xi}(i,j,k))}{\varepsilon_{xi}(i,j,k)}E_{inc,\,x}(i,j,k)-\frac{\kappa_{ex}(i,j,k)}{j\varepsilon_{xi}(i,\ j,\ ,k)c}\frac{1}{8}\\
&\left[\begin{array}{l}
+H_{inc,\,x}(i,j,k)+H_{inc,\,x}(i,\ j,\ k-1)\\
+H_{inc,\,x}(i+1,\ j,\ k)+H_{inc,\,x}(i+1,\ j,\ k-1)\\
+H_{inc,\,x}(i,\ j-1,\ k)+H_{inc,\,x}(i,\ j-1,\ k-1)\\
+H_{inc,\,x}(i+1,\ j-1,\ k)+H_{inc,\,x}(i+1,\ j-1,\ k-1)
\end{array}\right]
\end{aligned}
\tag{26a}
$$

$$
\begin{aligned}
&E_{scat,\,y}(i,j,k)+\frac{1}{j\omega\Delta x\varepsilon_{yx}(i,j,k)}H_{scat,\,z}(i,j,k)\\
&-\frac{1}{j\omega\Delta x\varepsilon_{yx}(i,j,k)}H_{scat,z}(i{-}1,j,k)-\frac{1}{j\omega\Delta z\varepsilon_{yz}(i,j,k)}H_{scat,x}(i,j,k)\\
&+\frac{1}{j\omega\Delta z\varepsilon_{yz}(i,j,k)}H_{scat,x}(i,j,k{-}1)+\frac{\kappa_{ey}(i,j,k)}{jc\varepsilon_{yi}(i,j,k)}\frac{1}{8}\\
&\left[\begin{array}{l}
+H_{scat,\,y}(i,j,k)+H_{scat,\,y}(i,\ j,\ k-1)\\
+H_{scat,\,y}(i,\ j+1,\ k)+H_{scat,\,y}(i,\ j+1,\ k-1)\\
+H_{scat,\,y}(i-1,\ j,\ k)+H_{scat,\,y}(i-1,\ j,\ k-1)\\
+H_{scat,\,y}(i-1,\ j+1,\ k)+H_{scat,\,y}(i-1,\ j+1,\ k-1)
\end{array}\right]
\end{aligned}
$$

$$= \frac{(\varepsilon_o - \varepsilon_{yi}(i,j,k))}{\varepsilon_{yi}(i,j,k)} E_{inc,\,y}(i,j,k) - \frac{\kappa_{ey}(i,j,k)}{jc\varepsilon_{yi}(i,j,k)} \frac{1}{8}$$
$$\left[ \begin{array}{l} +H_{inc,\,y}(i,j,k) + H_{inc,\,y}(i,\ j,\ k-1) \\ +H_{inc,\,y}(i,\ j+1,\ k) + H_{inc,\,y}(i,\ j+1,\ k-1) \\ +H_{inc,\,y}(i-1,\ j,\ k) + H_{scat,\,y}(i-1,\ j,\ k-1) \\ +H_{inc,\,y}(i-1,\ j+1,\ k) + H_{scat,\,y}(i-1,\ j+1,\ k-1) \end{array} \right] \quad (26b)$$

$$E_{scat,z}(i,j,k) - \frac{1}{j\omega\Delta x\varepsilon_{zx}(i,j,k)} H_{scat,\,y}(i,j,k)$$
$$+ \frac{1}{j\omega\Delta x\varepsilon_{zx}(i,j,k)} H_{scat,\,y}(i-1,j,k) + \frac{1}{j\omega\Delta y\varepsilon_{zy}(i,j,k)} H_{scat,x}(i,j,k)$$
$$- \frac{1}{j\omega\Delta y\varepsilon_{zy}(i,j,k)} H_{scat,\,x}(i,j-1,k) - \frac{j\kappa_{ez}(i,j,k)}{c\varepsilon_{zi}(i,j,k)} \frac{1}{8}$$
$$\left[ \begin{array}{l} +H_{scat,\,z}(i,j,k) + H_{scat,\,z}(i-1,\ j,\ k) \\ +H_{scat,\,z}(i,\ j-1,\ k) + H_{scat,\,z}(i-1,\ j-1,\ k) \\ +H_{scat,\,z}(i,\ j,\ k+1) + H_{scat,\,z}(i-1,\ j,\ k+1) \\ +H_{scat,\,z}(i,\ j-1,\ k+1) + H_{scat,\,z}(i-1,\ j-1,\ k+1) \end{array} \right]$$
$$= \frac{(\varepsilon_o - \varepsilon_{zi}(i,j,\kappa))}{\varepsilon_{zi}(i,j,k)} E_{inc,z}(i,j,k) + \frac{j\kappa_{ez}(i,j,k)}{c\varepsilon_{zi}(i,j,k)} \frac{1}{8}$$
$$\left[ \begin{array}{l} +H_{inc,\,z}(i,j,k) + H_{inc,\,z}(i-1,\ j,\ k) \\ +H_{inc,\,z}(i,\ j-1,\ k) + H_{inc,\,z}(i-1,\ j-1,\ k) \\ +H_{inc,\,z}(i,\ j,\ k+1) + H_{inc,\,z}(i-1,\ j,\ k+1) \\ +H_{inc,\,z}(i,\ j-1,\ k+1) + H_{inc,\,z}(i-1,\ j-1,\ k+1) \end{array} \right]. \quad (26c)$$

The positions of the material parameters ($\varepsilon$, $\mu$ and $\kappa$) are shown in Fig. 6. Notice that all values of $\varepsilon$ are associated with $\overline{E}$ field components, and all values of $\mu$ are associated with $\overline{H}$ field components. The $\kappa_e$'s are associated with $\overline{E}$ field components whereas the $\kappa_h$'s are associated with $\overline{H}$ field components.

The field components on the extended computational boundary are set to zero (i.e., a perfect electric conductor (PEC) wall is assumed at the outer side of the PML layers. The 6 field components in the interior nodes can be computed by solving the linear system of equations (25) to (26). For a problem consisting of $N$ Yee cells these equations can be arranged in a matrix form as $[A][EH] = [F]$ where $[A]$ is a $(6N \times 6N)$ coefficients matrix, $[EH]$ is the unknown vector of size $6N$ containing scattered $\overline{E}$ and $\overline{H}$ fields components, and $[F]$ is the excitation vector of size $6N$ representing the right hand side of equations (25) and (26), and they are a function of all incident field components. The coefficient matrix $[A]$ is a highly sparse matrix with

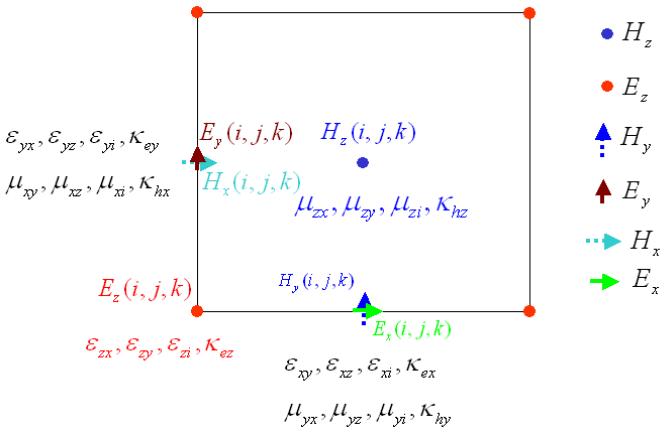


**Figure 6.** Position of the material parameters $\varepsilon$, $\mu$ and $\kappa$ in a face of one cell.

only 13 non-zero elements in each row, therefore only non-zero elements are stored while performing the matrix solution. It is not feasible to employ direct solution techniques in order to solve such very large sparse matrix equations. Iterative solvers such as BICGSTAB [12] are usually used in these cases. The numerical results obtained in this paper are based on our developed Fortran code based on the "vanilla" version of BiCGstab [13].

### 2.3. Accuracy and Computational Considerations

Spacing of the grid determines the accuracy and the cost of the computation. Therefore it is very critical to select the grid spacing, $\Delta x$, $\Delta y$ and $\Delta z$ properly in order to secure the accuracy of the computations without increasing the simulation time significantly. A good choice for selection of the grid spacing is to set it to be at most one-twentieth of the minimum wavelength of the frequency of interest, i.e.,

$$\Delta x_{\max},\ \Delta y_{\max},\ \text{and}\ \Delta z_{\max} \leq \frac{1}{20}\lambda_{\min} \tag{27a}$$

where

$$\lambda_{\min} = \frac{c}{f_{\max}\sqrt{\mu_{r\,\max}\varepsilon_{r\,\max}}} \tag{27b}$$

and $c$ is the speed of light in the free-space, $\mu_{r\,\max}$ and $\varepsilon_{r\,\max}$ are the maximum relative permeability and relative permittivity in the computational domain, and $f_{\max}$ indicates the maximum frequency of interest.

## 3. NUMERICAL RESULTS

### 3.1. Scattering from 3D Chiral Structures

In this section, the FDFD/PML solution procedure is applied to three-dimensional arbitrarily shaped chiral objects. The computer program is first validated by considering the case of scattering by a chiral sphere. The numerical solutions of the bistatic radar cross sections (the co-polarized bistatic radar cross section $\sigma_{\theta\theta}$ and the cross-polarized bistatic radar cross section $\sigma_{\phi\theta}$) are compared to the exact solutions for different material parameters. An analysis of the errors of the numerical solutions for the sphere is presented. To demonstrate that the proposed method is able to analyze a chiral body of arbitrary shape, the numerical solutions for a chiral cube and a finite circular chiral cylinder are also presented for various material parameters. All scatterers presented in this section are assumed to be illuminated by a $\theta$-polarized plane wave incident from the direction where $\theta_{inc} = 180°$ and $\varphi_{inc} = 0°$ ($\overline{E}_{inc} = -\hat{a}_x E_{inc} e^{-jk_o z}$, $\overline{H}_{inc} = -\hat{a}_y H_{inc} e^{-jk_o z}$, $E_{inc} = \eta_o H_{inc}$, $k_o$ and $\eta_o$ are the free space wavenumber and the intrinsic impedance respectively). The centers of all scatterers are at the origin. Figs. 7 to 10 show the geometries of the scatterers. Because the basic building block is a cube, curved surfaces on a scatterer are staircased. The size of the cubes is chosen to be at most $\lambda_{\min}/20$ of the maximum frequency of interest. As the cube size is decreased, it defines the geometry more accurate; however this can significantly increase the computational size of the problem.

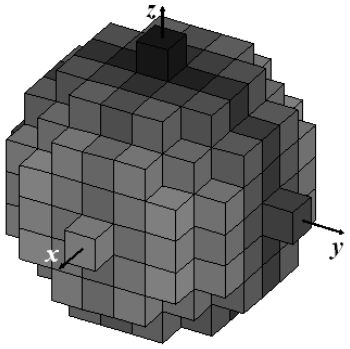


**Figure 7.** Coarse sphere constructed with relatively big cubes.

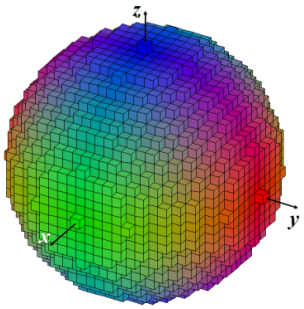


**Figure 8.** Fine sphere with small cubes.

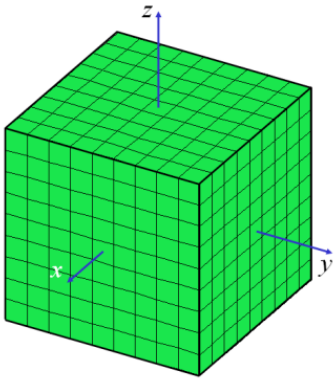


**Figure 9.** Cube constructed with smaller cubes.

### 3.2. Numerical Results for a Chiral Sphere

In this section, numerical solutions for scattering from a chiral sphere are presented. The solutions are compared to the exact solutions obtained by using the Matlab program presented in [14]. The problem to be investigated first is a sphere of radius 7.2 cm with parameters $\varepsilon_r = 4$ and $\mu_r = 1$. It is illuminated by a $z$-polarized, $x$-traveling plane wave at 1 GHz. The FDFD computational space is divided into 1 million ($100 \times 100 \times 100$) cubic cells where each cell is 0.25 cm on a side. Fig. 11 shows the co-polarized bistatic radar cross-sections, $\sigma_{\theta\theta}$ for $\kappa = 0$ (dielectric) and $\kappa = 0.5$. The cross-polarized bistatic radar cross-sections, $\sigma_{\phi\theta}$ for the same chirality parameters are shown in Fig. 12.

Field strengths of cross-polarized fields are generally very weak

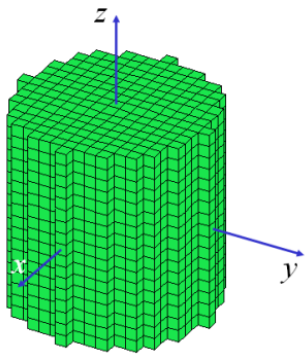


**Figure 10.** Finite length circular cylinder constructed with small cubes.

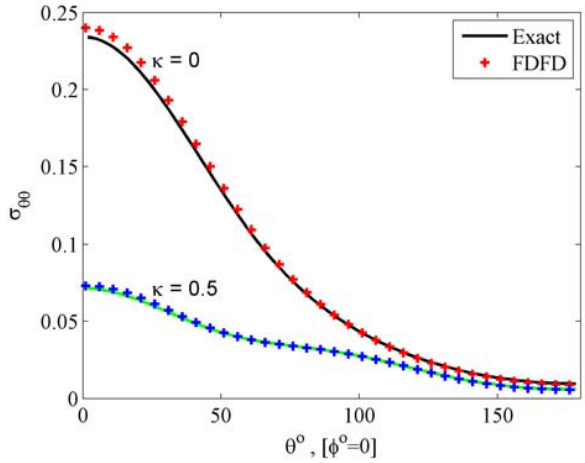


**Figure 11.** Scattering from a sphere, $\sigma_{\theta\theta}$ for $\kappa = 0$ and $\kappa = 0.5$.

compared to co-polarized components. Both co-polarized and cross-polarized field results show excellent agreement with the exact solution. Another remarkable observation in Figures 11 and 12 is that introducing the chirality into the sphere material gives rise to a cross-polarized field in the same order as the co-polarized field, which also exhibits the optical activity of the chiral media.

As the second case, scattering from a chiral sphere has been computed to study the convergence of the proposed method. Figures 13 and 14 show $\sigma_{\theta\theta}$ and $\sigma_{\phi\theta}$, respectively, for a chiral sphere with

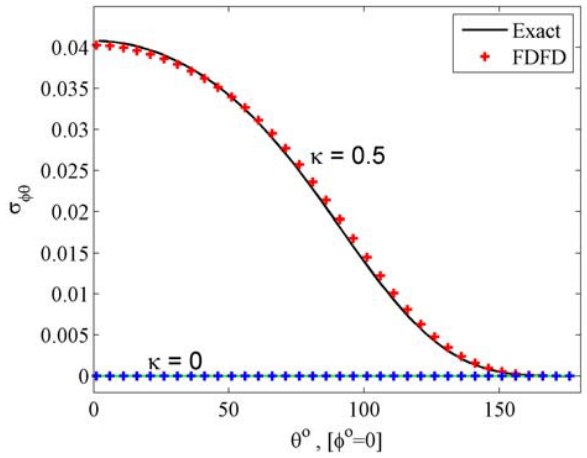


**Figure 12.** Scattering from a sphere, $\sigma_{\phi\theta}$ for $\kappa = 0$ and $\kappa = 0.5$.

parameters $\varepsilon_r = 4$, $\mu_r = 3$ and $\kappa = 0.5$. Figures 13 and 14 show the proof of convergence by comparing the numerical solutions with various cell sizes to the exact ones at 1 GHz. It has been observed that decreasing the cell size increases the accuracy and FDFD computation results converge to those given by the exact solutions.

### 3.3. Numerical Results for a Finite Circular Chiral Cylinder

In this section, the FDFD/PML procedure is applied to compute the co- and cross-polarized bistatic radar cross sections of a finite circular chiral cylinder. The results are compared to those obtained from the MoM [3] and FDTD [5] solutions. The cylinder is illuminated by an $x$-polarized, $z$ traveling plane wave at 1 GHz. The cylinder has 6 cm radius and 12 cm height. The cylinder material parameters are $\varepsilon_{DBR,r} = 4$, $\mu_{DBR,r} = 1$, and $\beta = 0.002$ given according to DBF constitutive relations [1]. The FDFD computational space is composed of 287,496 ($66 \times 66 \times 66$) cubic Yee cells of size 0.4 cm.

The co-polarized bistatic radar cross sections, $\sigma_{\theta\theta}$, are shown in Fig. 15. The cross-polarized bistatic radar cross sections, $\sigma_{\phi\theta}$, are shown in Fig. 16. The results show good agreement between FDFD and the MoM solutions. As one can see from these plots, cross-polarized scattering is significantly weaker than the co-polarized.

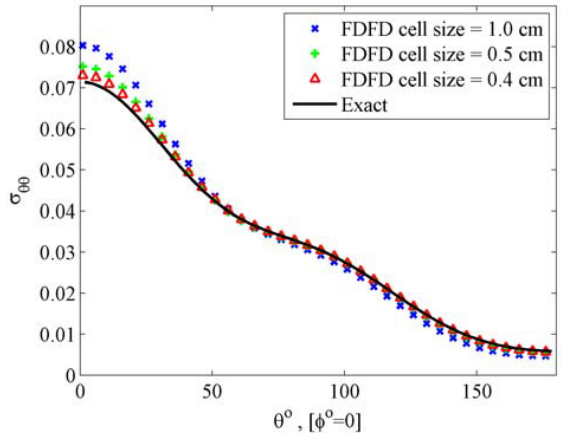


**Figure 13.** Convergence of computed $\sigma_{\theta\theta}$ to exact solution, $\kappa = 0.5$.

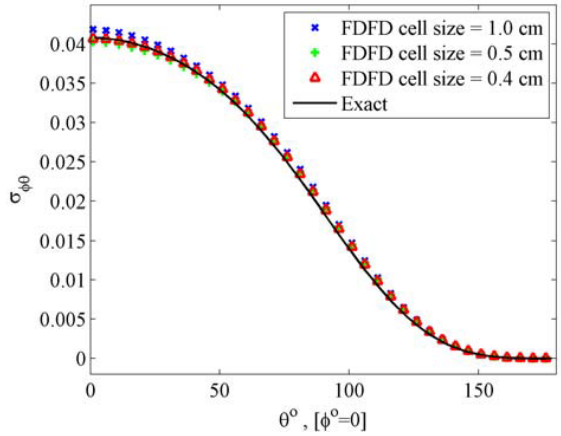


**Figure 14.** Convergence of computed $\sigma_{\phi\theta}$ to exact solution, $\kappa = 0.5$.

### 3.4. Numerical Results for a Chiral Cube

The developed FDFD formulation is used to calculate the co- and cross-polarized bistatic radar cross-sections of a chiral cube. The results are compared to those obtained from the MoM solution. Consider an $x$-polarized $z$-traveling incident plane wave at 1 GHz. The cube is 12 cm long on a side. The material parameters of the cube are given according to the DBF constitutive relations. The conversions in [1] are used to calculate the material parameter values in order to use in our solution.

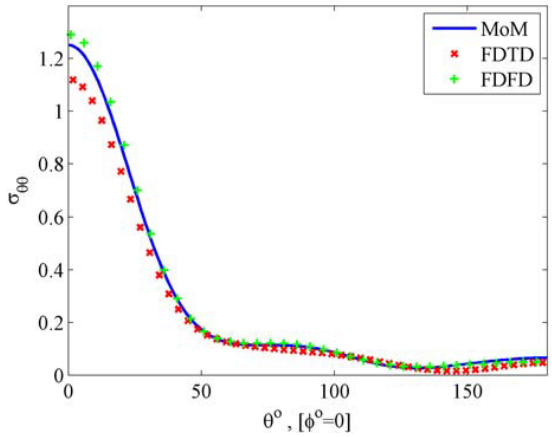


**Figure 15.** Scattering from a finite chiral cylinder, $\sigma_{\theta\theta}$ at 1 GHz.

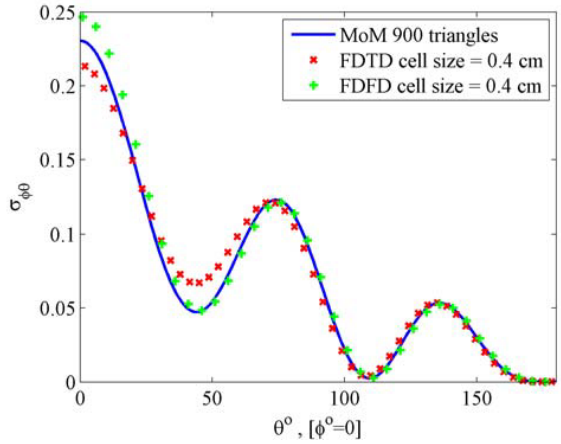


**Figure 16.** Scattering from a finite chiral cylinder, $\sigma_{\phi\theta}$ at 1 GHz.

The cube materials are $\varepsilon_{DBR,r} = 4$, $\mu_{DBF,r} = 1$ and $\beta = 0.0001$. The computational space is composed of 1 million ($100 \times 100 \times 100$) cubic Yee cells of size 0.25 cm.

The co-polarized bistatic radar cross section, $\sigma_{\theta\theta}$, is shown together with the reference solution in Fig. 17. The cross-polarized bistatic radar cross sections, $\sigma_{\phi\theta}$, is shown in Fig. 18. These graphs show good agreement with the MoM solutions.

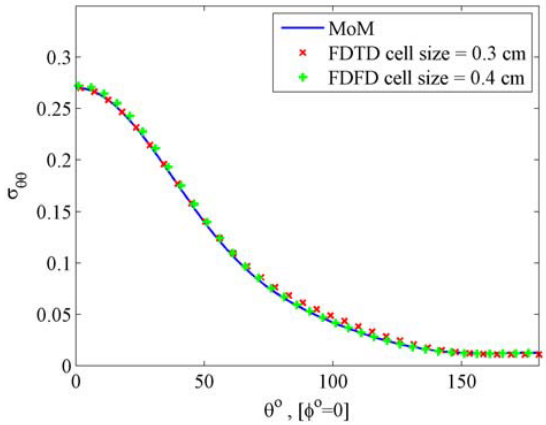


**Figure 17.** Scattering from a chiral cube, $\sigma_{\theta\theta}$ at 1 GHz.

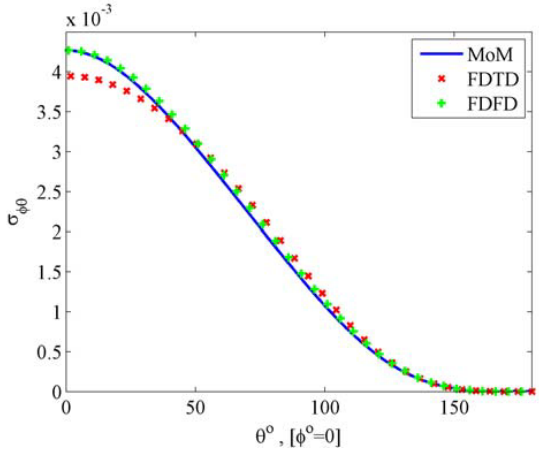


**Figure 18.** Scattering from a chiral cube, $\sigma_{\phi\theta}$ at 1 GHz.

## 4. CONCLUSIONS

The FDFD formulation of scattering from 3D arbitrarily shaped chiral objects has been developed in this paper. First, numerical results for chiral sphere has been presented and compared to the exact results. Excellent agreement between the numerically generated results and the exact results has been observed. Second, numerical results for radar cross sections are presented for circular chiral cylinders of different size and material parameters. The excellent agreement between the

numerically generated results and the exact results for several chiral cylinders of different parameters and different wave incidence shows the validity and the accuracy of the FDFD method developed in this paper. The effect of chirality on the internal and external fields can be noticed in the examples of scattering by the chiral cylinders as compared to the achiral cylinders for different chirality parameters. Adding chirality to the cylinder causes the cross-polarized field component to change significantly. This demonstrates the increasing shift of the polarization of the scattered field as compared to the incident wave.

More results examining the interaction of electromagnetic fields with chiral objects are presented through the examples of scattering from a variety of chiral cylinders of different geometrical shape and material parameters. The effect of adding chirality to the scatterer on the internal fields is to generate a cross-polarized component and also to change the pattern of the co-polarized component. This in turn results in the rotation of polarization in the scattered far fields, which is characteristic of the chiral materials.

## REFERENCES

1. Lindell, I. V., A. H. Sihvola, S. A. Tretyakov, and A. J. Viitanen, *Electromagnetic Waves in Chiral and Bi-isotropic Media*, Artech House, Boston and London, 1994.
2. Al-Kanhal, M. A. and E. Arvas, "Electromagnetic scattering from a chiral cylinder of arbitrary cross section," *IEEE Trans. Antennas and Propagat.*, Vol. 44, No. 7, 1041–1048, July 1996.
3. Worasawate, D., J. R. Mautz, and E. Arvas, "Electromagnetic scattering from an arbitrarily shaped three-dimensional homogeneous chiral body," *IEEE Transactions on Antennas and Propagation*, Vol. 51, No. 5, 1077–1084, May 2003.
4. Akyurtlu, A. and D. H. Werner, "Novel dispersive FDTD formulation for modeling transient propagation in chiral metamaterials," *IEEE Transactions on Antennas and Propagation*, Vol. 52, No. 9, 2267–2276, September 2004.
5. Demir, V., A. Z. Elsherbeni, and E. Arvas, "FDTD formulation for dispersive chiral media using the $Z$ transform method," *IEEE Transactions on Antennas and Propagation*, Vol. 53, No. 10, 3374–3384, October 2005.
6. Elsherbeni, A. Z., M. H. Al Sharkawy, and S. F. Mahmoud, "Electromagnetic scattering from a 2D chiral strip simulated by circular cylinders for uniform and non-uniform chirality

distribution," *IEEE Transactions on Antennas and Propagation*, Vol. 52, No. 9, 2244–2252, September 2004.

7. Berenger, J., "A perfectly matched layer of the absorption of electromagnetic waves," *J. Comp. Phys.*, Vol. 114, No. 2, 185–200, October 1994.
8. Kunz, K. S. and R. J. Luebbers, *The Finite Difference Time Domain Method for Electromagnetics*, CRC Press, 1993.
9. Taflove, A. and S. C. Hagness, *Computational Electrodynamics: the Finite Difference Time-domain Method*, 2nd edition, Artech House, Norwood, MA, 2000.
10. Al Sharkawy, M. H., V. Demir, and A. Z. Elsherbeni, "Iterative multi-region technique for large scale electromagnetic scattering problems—two dimensional case," *Radio Science*, Vol. 40, No. 5, September 2005.
11. Yee, K. S., "Numerical solution of initial boundary value problems involving Maxwell's equations in isotropic media," *IEEE Transactions on Antennas and Propagation*, Vol. AP-14, 302–307, 1966.
12. Van der Vorst, H. A., "Bi-CGSTAB: a fast and smoothly converging variant of Bi-CG for the solution of nonsymmetric linear systems," *SIAM J. Sci. Stat. Comput.*, Vol. 13, No. 2, 631–644, 1992.
13. Sleijpen, G. L. G. and D. R. Fokkema, "BiCGstab(l) for linear equations involving unsymmetric matrices with complex spectrum," *Electronic Transactions on Numerical Analysis (ETNA)*, Vol. 1, 11–32, 1993.
14. Demir, V., A. Elsherbeni, D. Worasawate, and E. Arvas, "A graphical user interface (GUI) for plane-wave scattering from a conducting, dielectric, or chiral sphere," *IEEE Antennas and Propagation Magazine*, Vol. 46, No. 5, 94–99, Oct. 2004.